

Binding of curvature-inducing proteins onto tethered vesicles

Hiroshi Noguchi*

Institute for Solid State Physics, University of Tokyo, Kashiwa, Chiba 277-8581, Japan

(Dated: September 21, 2021)

A tethered vesicle, which consists of a cylindrical membrane tube and a spherical vesicle, is produced by a mechanical force that is experimentally imposed by optical tweezers and a micropipette. This tethered vesicle is employed for examining the curvature sensing of curvature-inducing proteins. In this study, we clarify how the binding of proteins with a laterally isotropic spontaneous curvature senses and generates the membrane curvatures of the tethered vesicle using mean-field theory and meshless membrane simulation. The force-dependence curves of the protein density in the membrane tube and the tube curvature are reflection symmetric and point symmetric, respectively, from the force point, in which the tube has a sensing curvature. The bending rigidity and spontaneous curvature of the bound proteins can be estimated from these force-dependence curves. First-order transitions can occur between low and high protein densities in the tube at both low and high force amplitudes. The simulation results of the homogeneous phases agree very well with the theoretical predictions. In addition, beaded-necklace-like tubes with microphase separation are found in the simulation.

I. INTRODUCTION

In living cells, numerous protein types work together to regulate biomembrane shapes [1–6]. Proteins are also involved in various dynamical processes, such as end/exocytosis and vesicle transport. The Bin/Amphiphysin/Rvs (BAR) superfamily proteins bend the membrane along its axis and generate cylindrical membrane tubes [1–3, 7, 8]. Other proteins, such as clathrin and coat protein complex (COPI and COPII), generate spherical buds [3–6]. Thus, understanding the mechanism of these curvature generations is important.

These curvature-inducing proteins are known to sense the membrane curvature and are concentrated in membranes which have their preferred curvatures. Various types of proteins can be examined using a tethered vesicle pulled by optical tweezers and a micropipette [9–15]. With increasing force or length, the vesicle first deforms into a lemon shape and subsequently forms a narrow membrane tube (tether) protruding from a spherical vesicle [16–18]. Moreover, an elongational force can be produced by the growth of protein filaments *in vitro* [16, 19] and *in vivo* [20, 21]. Curvature-inducing proteins typically bind more onto the membrane tube than the remaining spherical component. BAR proteins [10–12], dynamin [13], and G-protein coupled receptors [14] have been reported to exhibit curvature sensing.

The aim of this study is to understand the curvature sensing and generation of the curvature-inducing proteins with an isotropically spontaneous curvature on a tethered vesicle. We employ mean-field theory and meshless membrane simulation. In mean-field theory, a simplified geometry is considered for vesicles. Previously, we used a vesicle consisting of many spherical components to study budding [22]. Here, we apply the same scheme to the tethered vesicle. Although mean-field theories have been

used to analyze the experimental results of tethered vesicles [12, 14], they have been applied in narrow ranges of the parameters, and the curvature of the spherical component has not been considered. Here, we systematically investigate the protein binding onto the tethered vesicle over a wide range of parameters.

Several types of membrane models have been developed for coarse-grained simulations [23–25]. For a large-scale simulation, we developed two types of meshless membrane models [26, 27], in which membrane particles self-assemble into a single-layer membrane and the mechanical properties can be varied over a wide range. Here, we employ a spin meshless membrane model [27], since it can vary the spontaneous curvature and has been applied to membrane deformation by curvature-inducing proteins with an isotropic spontaneous curvature [28, 29] and with an anisotropic spontaneous curvature [30–35], as well as topological changes of membranes [36, 37]. In mean-field theory, we assume a uniform distribution of the bound proteins in each membrane component. However, phase separation has been obtained in simulations of membrane tubes [28] and flat membranes [29]. We clarify where the phase separation of the bound proteins occurs in the membrane tubes under a constant external force and where the assumption of uniform protein density is valid.

The mean-field theory of the tethered vesicle is described in Sec. II. Simulations of membrane tubes are described in Sec. III. The simulation results are compared with the theoretical results in Sec. III B. Finally, a summary and discussion are presented in Sec. IV.

II. TETHERED VESICLE

A. Mean-Field Theory

A vesicle consists of a sphere with radius R_{sp} and a cylinder with radius R_{cy} and length L_{cy} as depicted in

* noguchi@issp.u-tokyo.ac.jp

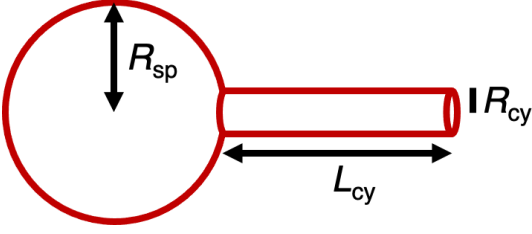


FIG. 1. Simplified geometry of a tethered vesicle. The vesicle consists of a sphere with a radius R_{sp} and a cylinder with a radius R_{cy} and length L_{cy} .

Fig. 1. Here, a thin tube of $R_{cy} \ll R_{sp}$ is considered, such that the end and foot parts of the cylindrical tube are neglected. This geometry was previously used in Ref. 38. In experiments, the end shape of the tube can be strongly affected by force-imposing methods such as optical tweezers, whereas the foot has a catenoid-like shape with a low mean-curvature [39].

The total surface area A and volume V are given as follows:

$$A = 4\pi R_0^2 = 4\pi R_{sp}^2 + 2\pi R_{cy}L_{cy}, \quad (1)$$

$$V = \frac{4\pi}{3}R_{sp}^3 + \pi R_{cy}^2L_{cy}, \quad (2)$$

where R_0 is the radius of a sphere with the same surface area. From Eqs. (1) and (2), the radius and length of the membrane tube can be expressed as follows:

$$\frac{R_{cy}L_{cy}}{R_0^2} = 2(1 - r^2), \quad (3)$$

$$\frac{R_{cy}}{R_0} = \frac{2(v_r - r^3)}{3(1 - r^2)}, \quad (4)$$

where $r = R_{sp}/R_0$ and reduced volume $v_r = V/(4\pi R_0^3/3)$.

Curvature-inducing proteins bind to the membrane, depending on the local membrane curvature. The bending free energy F_{cv} is given by

$$F_{cv} = \int dA \left\{ 2\kappa_d H^2(1 - \phi) + \frac{\kappa_p}{2}(2H - C_0)^2\phi \right\}, \quad (5)$$

where H is the mean curvature of the membrane ($H = (C_1 + C_2)/2$, where C_1 and C_2 are the principal curvatures). The first and second terms represent the bending energy of the bare (unbound) and protein-bound membranes, respectively, and ϕ is the protein density ($\phi = 1$ at the maximum coverage). The unbound membrane has bending rigidity κ_d and zero spontaneous curvature; the bound membrane has a larger bending rigidity κ_p and spontaneous curvature C_0 . In this study, the effects of the saddle-splay modulus $\bar{\kappa}$ are not considered. Although $\bar{\kappa}$ may depend on the protein density, the cylindrical membrane has zero Gaussian curvature ($C_1 C_2$) such that it has no influence in the middle of the tube. Small effects may appear through the neglected regions (the end and

foot of the membrane tube). More general aspects of the protein-binding model are discussed in Ref. [22].

To induce a tether (thin membrane tube), an external force f_{ex} is imposed. Here, it is assumed that the proteins are homogeneously distributed in each membrane component (the spherical or cylindrical component). The subscripts sp and cy represent the quantities of spherical and cylindrical components of the vesicle, respectively. The free energy F of the tethered vesicle is given by

$$F = F_{sp} + F_{cy} - f_{ex}(L_{cy} + 2R_{sp}), \quad (6)$$

$$\begin{aligned} \frac{F_{sp}}{4\pi} &= 2(\kappa_{dif}\phi_{sp} + \kappa_d) - 2\kappa_p C_0 R_0 r \phi_{sp} \\ &\quad + R_0^2 r^2 (\sigma_p \phi_{sp} + b\phi_{sp}^2) \\ &\quad + \frac{k_B T R_0^2 r^2}{a_p} [\phi_{sp} \ln(\phi_{sp}) + (1 - \phi_{sp}) \ln(1 - \phi_{sp})], \end{aligned} \quad (7)$$

$$\begin{aligned} \frac{F_{cy}}{\pi} &= (\kappa_{dif}\phi_{cy} + \kappa_d) \frac{L_{cy}}{R_{cy}} - 2\kappa_p C_0 L_{cy} \phi_{cy} \\ &\quad + 2R_{cy}L_{cy} \left\{ (\sigma_p \phi_{cy} + b\phi_{cy}^2) \right. \\ &\quad \left. + \frac{k_B T}{a_p} [\phi_{cy} \ln(\phi_{cy}) + (1 - \phi_{cy}) \ln(1 - \phi_{cy})] \right\} \\ &= (\kappa_{dif}\phi_{cy} + \kappa_d) \frac{9(1 - r^2)^3}{2(v_r - r^3)^2} - 6\kappa_p C_0 R_0 \frac{(1 - r^2)^2 \phi_{cy}}{v_r - r^3} \\ &\quad + 4(1 - r^2) R_0^2 \left\{ (\sigma_p \phi_{cy} + b\phi_{cy}^2) \right. \\ &\quad \left. + \frac{k_B T}{a_p} [\phi_{cy} \ln(\phi_{cy}) + (1 - \phi_{cy}) \ln(1 - \phi_{cy})] \right\}, \end{aligned} \quad (8)$$

where $\kappa_{dif} = \kappa_p - \kappa_d$ and $\sigma_p = -\mu/a_p + \kappa_p C_0^2/2$. The chemical potential of the protein binding is μ , and a_p is the membrane area bound by one protein. The last terms in Eqs. (7)–(9) represent the mixing entropy of the bound proteins. The inter-protein interactions are taken into account as squared density terms of $b\phi^2$. Proteins have repulsive or attractive interactions at $b > 0$ and $b < 0$, respectively.

The densities ϕ_{sp} and ϕ_{cy} are obtained from $\partial F/\partial\phi|_H = 0$:

$$\phi = \frac{1}{1 + \exp \left[\frac{a_p}{k_B T} (2\kappa_{dif} H^2 - 2\kappa_p C_0 H + \sigma_p + 2b\phi) \right]}, \quad (10)$$

where $H = 1/R_{sp}$ and $H = 1/2R_{cy}$ for the spherical and cylindrical components, respectively [22]. For $b = 0$, this is a sigmoid function of μ . For $b \neq 0$, Eq. (10) is iteratively solved with an updated ϕ value in the right hand side. Thus, the free energy F is expressed as a function of one variable r using Eqs. (7) and (9) with ϕ_{sp} and ϕ_{cy} obtained using Eq. (10). Hence, the free-energy minimum is calculated by $\partial F/\partial r = 0$.

The maximum binding (sensing) of the proteins occurs at a higher density than the curvature generation [22]. The curvatures of sensing and generation are obtained by $\partial\phi/\partial H = 0$ and $\partial F/\partial H = 0$ at $f_{ex} = 0$, respectively. The sensing curvature is $H_s = \kappa_p C_0/2\kappa_{dif}$, and the curvature of the generation is $H_g = \kappa_p \phi C_0/2(\kappa_{dif}\phi + \kappa_d)$.

Hence, the maximum protein density ϕ_{cy}^{\max} is obtained at $1/R_{cy} = C_s = \kappa_p C_0 / \kappa_{dif}$ for the cylindrical tube, $\phi_{cy}^{\max} = 1 / \{1 + \exp[-(\mu - \mu_0) / k_B T]\}$ at $b = 0$, where $\mu_0 = -a_p \kappa_p C_0^2 (\kappa_p / \kappa_{dif} - 1) / 2$. At $\mu = \mu_0$, $\phi_{cy}^{\max} = 1/2$ is obtained. In the dilute limit $\phi_{sp} \ll 1$ and $\phi_{sp} \ll 1$ with $R_{sp} \gg R_{cy}$ and $b = 0$, the density ratio is given by

$$\frac{\phi_{cy}}{\phi_{sp}} \simeq \exp \left\{ - \frac{\kappa_{dif} a_p}{2 k_B T} \left[\left(\frac{1}{R_{cy}} - C_s \right)^2 - C_s^2 \right] \right\}, \quad (11)$$

as reported in Ref. 12.

The surface tension σ_d and osmotic pressure Π can be expressed as Lagrange multipliers to maintain the area and volume, respectively: $\tilde{F} = F + \sigma_d A - \Pi V$. Then, σ_d , Π , and f_{ex} satisfy $\partial \tilde{F} / \partial R_{sp} |_{R_{cy}, L_{cy}} = 0$, $\partial \tilde{F} / \partial R_{cy} |_{R_{sp}, L_{cy}} = 0$, and $\partial \tilde{F} / \partial L_{cy} |_{R_{sp}, R_{cy}} = 0$:

$$\Pi = \frac{f_{ex}}{\pi R_{cy}^2} - \frac{2(\kappa_{dif} \phi_{cy} + \kappa_d)}{R_{cy}^3} + \frac{2\kappa_p C_0 \phi_{cy}}{R_{cy}^2}, \quad (12)$$

$$\begin{aligned} \sigma_d &= \Pi R_{cy} + \frac{\kappa_{dif} \phi_{cy} + \kappa_d}{2 R_{cy}^2} - \sigma_p \phi_{cy} - b \phi_{cy}^2 \\ &\quad - \frac{k_B T}{a_p} [\phi_{cy} \ln(\phi_{cy}) + (1 - \phi_{cy}) \ln(1 - \phi_{cy})] \\ &= \frac{\Pi R_{sp}}{2} + \frac{f_{ex}}{4\pi R_{sp}} + \frac{\kappa_p C_0 \phi_{sp}}{R_{sp}} - \sigma_p \phi_{sp} - b \phi_{sp}^2 \\ &\quad - \frac{k_B T}{a_p} [\phi_{sp} \ln(\phi_{sp}) + (1 - \phi_{sp}) \ln(1 - \phi_{sp})]. \end{aligned} \quad (13)$$

The first terms in Eqs. (13) and (14) represent the Laplace tensions. Here, the spherical and cylindrical components share the same surface tension, which is different from the analysis in Ref. [12]. Because lipid molecules can freely move between these components, their surface tension is balanced.

When the volume of the cylindrical tube is negligibly small as $R_{cy}^2 L_{cy} / R_0^3 \ll 1$, the spherical component can be approximated to have a maximum volume of $V = 4\pi R_{sp}^3 / 3$. In this limit condition [38], the following relation is obtained:

$$r \simeq v_r^{1/3}, \quad (15)$$

$$\frac{R_{cy} L_{cy}}{R_0^2} \simeq 2(1 - v_r^{2/3}). \quad (16)$$

Smith et al. reported that this approximation reproduces the force-length relation of tethered vesicles with zero spontaneous curvature [38]. In this approximation, L_{cy} is a variable, whereas r is a constant. We call this approximation limit analysis and use sub- or superscripts *lim* to represent the quantities calculated by this method. The vesicle shape is obtained from $\partial F / \partial L_{cy} = 0$, as

$$f_{ex} \simeq \frac{\pi(\kappa_{dif} \phi_{cy} + \kappa_d) L_{cy}}{(1 - v_r^{2/3}) R_0^2} - 2\pi \kappa_p C_0 \phi_{cy} \quad (17)$$

$$= \frac{2\pi(\kappa_{dif} \phi_{cy} + \kappa_d)}{R_{cy}} - 2\pi \kappa_p C_0 \phi_{cy} \quad (18)$$

$$= \left[\left(\frac{\kappa_{dif}}{\kappa_d} \phi_{cy} + 1 \right) \left(\frac{1}{R_{cy} C_s} - 1 \right) + 1 \right] f_s, \quad (19)$$

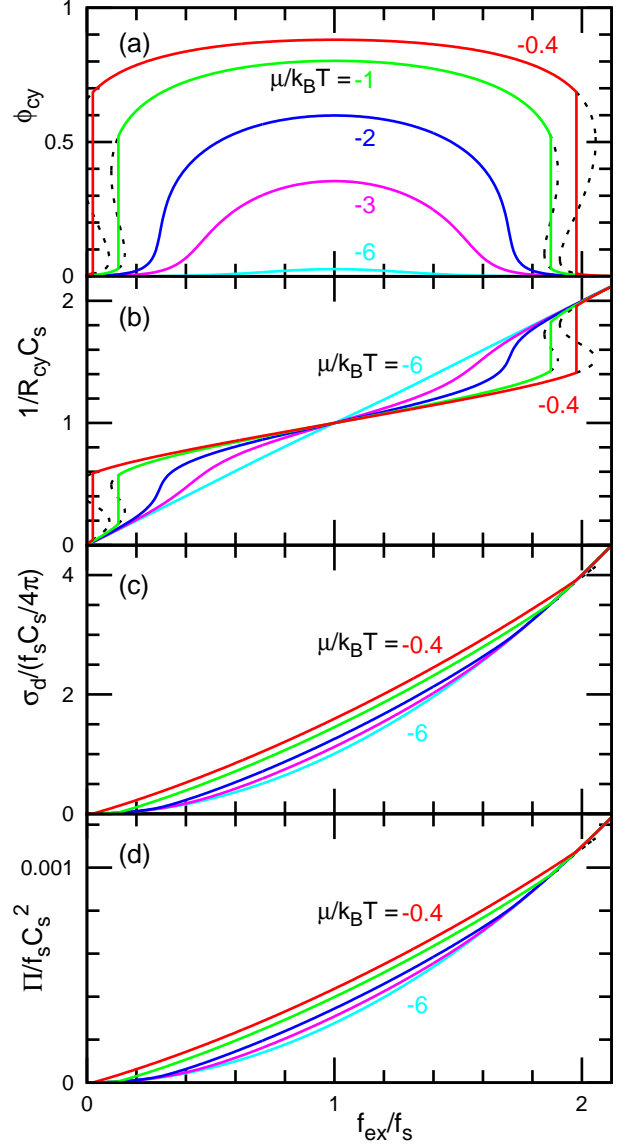


FIG. 2. Force f_{ex} dependence of (a) the protein density ϕ_{cy} and (b) curvature $1/R_{cy}$ of the cylindrical membrane, (c) the surface tension σ_d , and (d) the osmotic pressure Π for $\mu/k_B T = -6, -3, -2, -1,$ and -0.4 at $C_0 R_0 = 400$, $v_r = 0.9$, $\kappa_p / \kappa_d = 3$, and $b = 0$. The solid lines represent thermal equilibrium states. The dashed lines represent the metastable and free-energy-barrier states. From the bottom to top, $\mu/k_B T = -6, -3, -2, -1,$ and -0.4 in (a), (c), and (d).

where $f_s = 2\pi \kappa_d C_s$. The maximum protein density is obtained at $f_{ex} = f_s$, since $1/R_{cy} = C_s$ at the maximum. The force f_{ex} linearly increases with the tube curvature $1/R_{cy}$ for a constant ϕ_{cy} . In particular, for completely unbound tubes ($\phi_{cy} = 0$), f_{ex} is proportional to $1/R_{cy}$ as $f_{ex}/f_s \simeq 1/R_{cy} C_s$. For any value of ϕ_{cy} , $f_{ex} = f_s$ at $R_{cy} C_s = 1$. The surface tension σ_d is obtained from

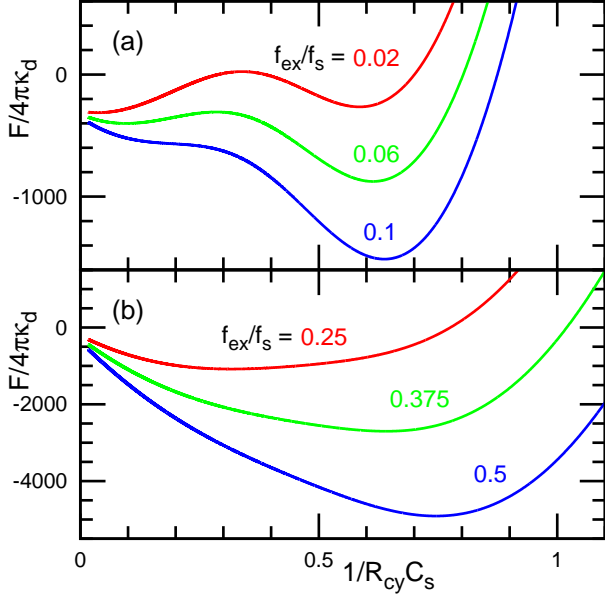


FIG. 3. Free energy profile at $C_0R_0 = 400$, $v_r = 0.9$, $\kappa_p/\kappa_d = 3$, and $b = 0$. (a) $\mu/k_B T = -0.4$. (b) $\mu/k_B T = -2$. The free energy has a double minima at $f_{ex}/f_s = 0.02$ and 0.06 in (a).

$\partial \check{F} / \partial R_{cy} |_{L_{cy}} = 0$ with $\check{F} = F + \sigma_d A$:

$$\sigma_d \simeq \frac{\kappa_{dif} \phi_{cy} + \kappa_d}{2R_{cy}^2} - \sigma_p \phi_{cy} - b \phi_{cy}^2 - \frac{k_B T}{a_p} [\phi_{cy} \ln(\phi_{cy}) + (1 - \phi_{cy}) \ln(1 - \phi_{cy})]. \quad (20)$$

Hence, the first term in Eq. (13) is neglected in the limit analysis. For completely unbound membrane tubes of $\phi_{cy} = 0$, a well-known relation $\sigma_d = \kappa_d / 2R_{cy}^2 = f_{ex} / 4\pi R_{cy}$ is obtained. This relation has been used to estimate R_{cy} and κ_d from σ_d and f_{ex} experimentally [9, 40–42]. However, the surface tension of the bound membranes exhibits a more complicated dependence, as expressed in Eq. (20). As described in Sec. II B, this limit method provides a good approximation for thin tubes.

We use $\kappa_d = 20k_B T = 8 \times 10^{-20}$ J, $a_p = 100$ nm², and $R_0 = 10$ μ m, i.e., $a_p/R_0^2 = 10^{-6}$. External forces are typically at $f_{ex} \sim 10$ pN, which can be imposed using optical tweezers. For $C_s = 100/R_0 = 10^7$ m⁻¹, $f_s = 2\pi\kappa_d C_s \simeq 5$ pN. In the plots, the data at $R_{cy}/R_0 < 0.1$ are displayed (i.e., too wide tubes are excluded). In this study, the iterations of the density calculation for $b \neq 0$ were repeated until the difference in ϕ was less than 10^{-8} ; fewer than ten iterations were typically performed.

B. Theoretical Results

In this subsection, we describe the results of the mean-field theory using the simplified geometry depicted in Fig. 1. Figures 2–4 and Figs. 5–6 show the results at $C_0R_0 = 400$ and $C_0R_0 = 100$, respectively, at $v_r = 0.9$,

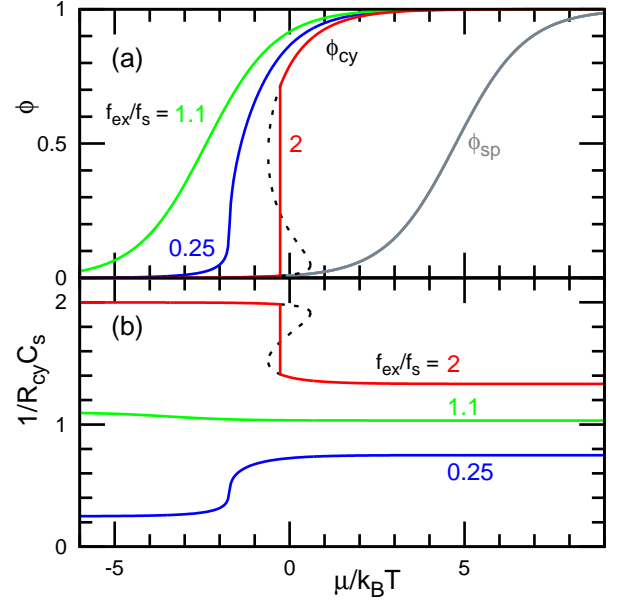


FIG. 4. Chemical potential μ dependence of (a) the protein densities ϕ and (b) the curvature $1/R_{cy}$ of the cylindrical membrane for $f_{ex}/f_s = 0.25, 1.1, \text{ and } 2$ at $C_0R_0 = 400$, $v_r = 0.9$, $\kappa_p/\kappa_d = 3$, and $b = 0$. The solid lines represent thermal equilibrium states. The dashed lines represent the metastable and free-energy-barrier states. The gray line in (a) represents ϕ_{sp} (all data for $f_{ex}/f_s = 0.25, 1.1, \text{ and } 2$ overlap this single curve).

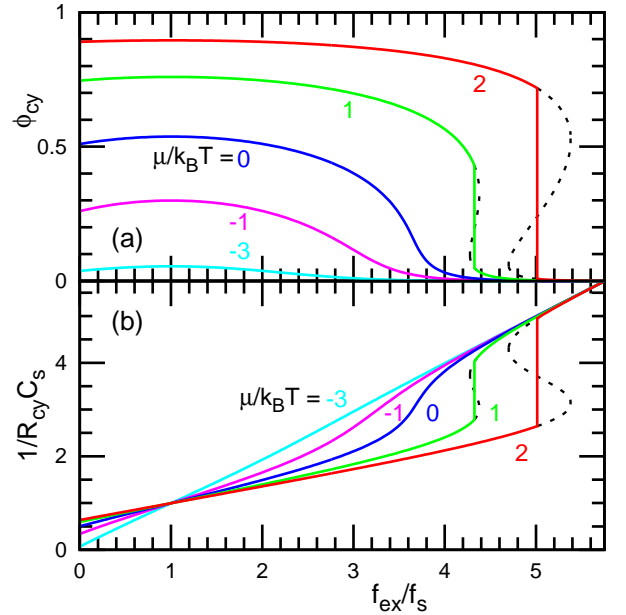


FIG. 5. Force f_{ex} dependence of (a) the protein density ϕ_{cy} and (b) curvature $1/R_{cy}$ of the cylindrical membrane for $\mu/k_B T = -3, -1, 0, 1, \text{ and } 2$ at $C_0R_0 = 100$, $v_r = 0.9$, $\kappa_p/\kappa_d = 3$, and $b = 0$. The solid lines represent thermal equilibrium states. The dashed lines represent the metastable and free-energy-barrier states.

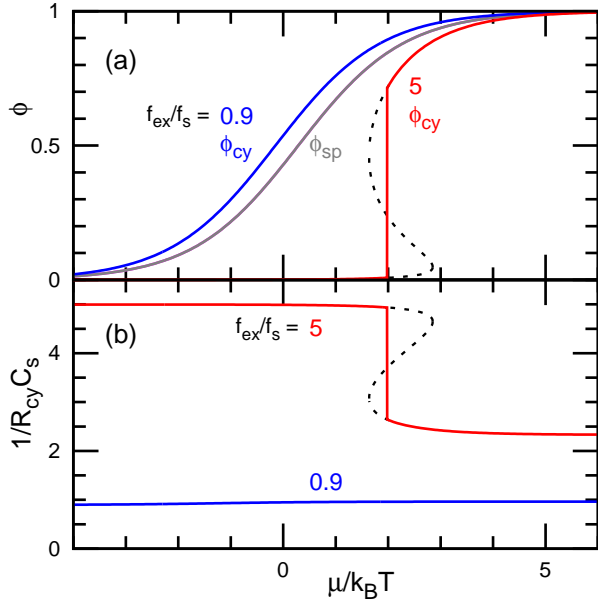


FIG. 6. Chemical potential μ dependence of (a) the protein densities ϕ and (b) the curvature $1/R_{cy}$ of the cylindrical membrane for $f_{ex}/f_s = 0.9$ and 5 at $C_0 R_0 = 100$, $v_r = 0.9$, $\kappa_p/\kappa_d = 3$, and $b = 0$. The solid lines represent thermal equilibrium states. The dashed lines represent the metastable and free-energy-barrier states. The gray line in (a) represents ϕ_{sp} (both data for $f_{ex}/f_s = 0.9$ and 5 overlap this single curve).

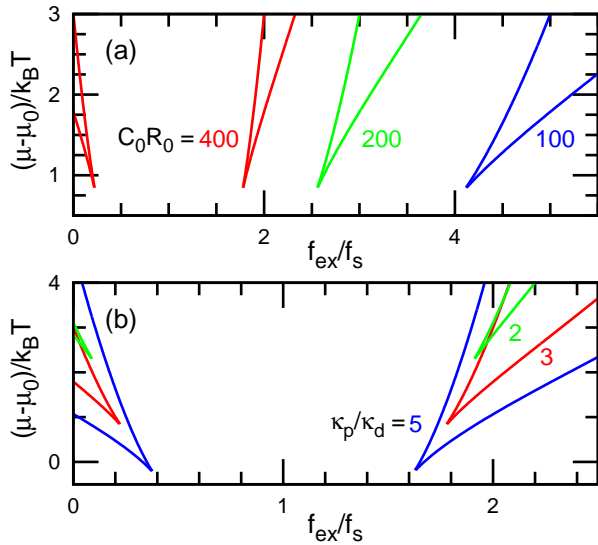


FIG. 7. Phase diagrams at $v_r = 0.9$ and $b = 0$. Two states with narrow and wide tubes coexist in the region between the two solid lines. (a) $C_0 R_0 = 100, 200,$ and 400 at $\kappa_p/\kappa_d = 3$. (b) $\kappa_p/\kappa_d = 2, 3,$ and 5 at $C_0 R_0 = 400$. The origin of the chemical potential is at μ_0 to give $\phi_{cy} = 0.5$ at $f_{ex}/f_s = 1$.

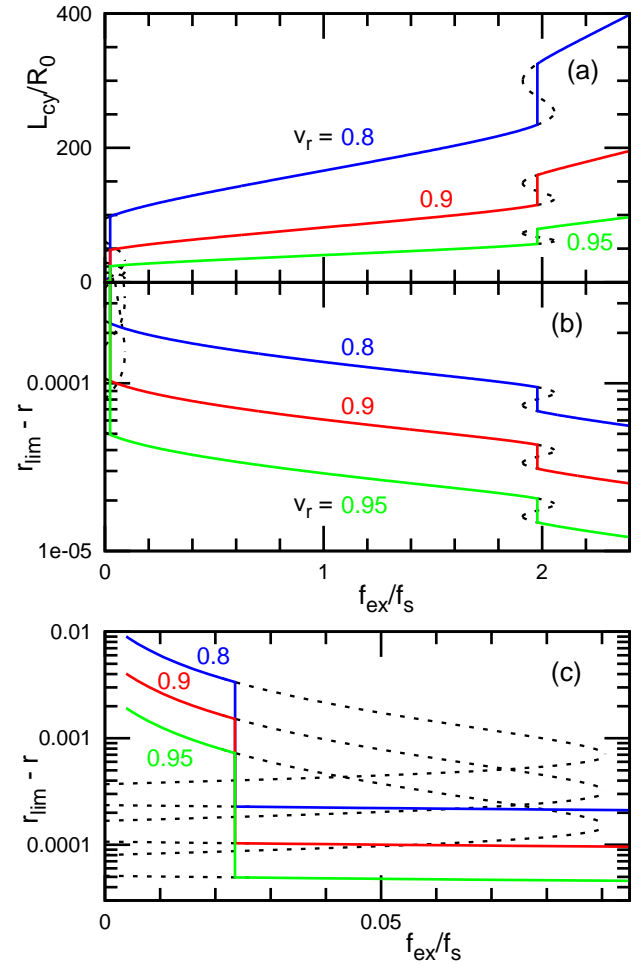


FIG. 8. Effects of reduced volume v_r at $C_0 R_0 = 400$, $\mu/k_B T = -0.4$, $\kappa_p/\kappa_d = 3$, and $b = 0$. (a) Length of the cylindrical membrane for $v_r = 0.8, 0.9,$ and 0.95 . (b),(c) Difference of radius of the spherical membrane from the maximum value r_{lim} for (b) large and (c) small f_{ex} regions. The solid lines represent thermal equilibrium states. The dashed lines represent the metastable and free-energy-barrier states.

$\kappa_p/\kappa_d = 3$, and $b = 0$. When the proteins are unbound at a low chemical potential μ , the tube curvature is proportional to the force strength, as shown in Figs. 2(b) and 5(b). As μ increases, the protein density ϕ_{cy} increases, so that the force curve changes, as predicted in Eqs. (10) and (19). The force dependence curves of ϕ_{cy} are visually reflection symmetric with respect to $f_{ex}/f_s = 1$ and take the maxima at $f_{ex}/f_s = 1$ as shown in Figs. 2(a) and 5(a). The tube curvature $1/R_{cy}$ is point symmetric with respect to $f_{ex}/f_s = 1$ (see Figs. 2(b) and 5(b)). Thus, the results are reproduced well by the limit analysis using $r = v_r^{1/3}$. When C_0 and κ_p are unknown, they can be estimated from the tube radius at the maximum value of ϕ_{cy} and the slope of $d(1/R_{cy})/df_{ex} = 1/2\pi(k_{dif}\phi_{cy}^{max} + k_d)$ at $f_{ex}/f_s = 1$, respectively.

For large μ , first-order transitions occur between the unbound and bound tubes with different tube radii (see

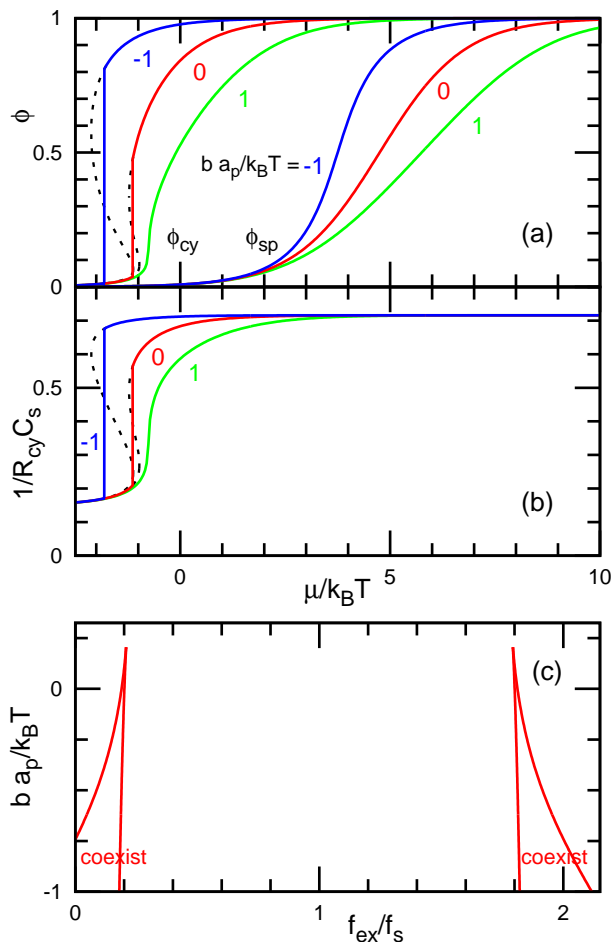


FIG. 9. Dependence on pairwise interactions at $C_0 R_0 = 400$, $v_r = 0.9$, and $\kappa_p/\kappa_d = 3$. (a) Protein densities ϕ_{cy} and ϕ_{sp} of the cylindrical and spherical membrane components, respectively, for $ba_p/k_B T = -1, 0$, and 1 at $f_{ex}/f_s = 0.15$. (c) Phase diagrams at $\mu/k_B T = -1.5$. Two states with narrow and wide tubes coexist in the region between the two solid lines.

Figs. 2 and 5). These transitions appear symmetrically with both small and large f_{ex} with respect to $f_{ex}/f_s = 1$. Around the transition points, the free energy profile has two minima (see Fig. 3), so that the unbound and bound states coexist (see van der Waals loop depicted by the dashed lines in Figs. 2 and 5). These two transitions can be understood using Eq. (19) of the limit analysis; at large μ , Eq. (19) has two regions of $df_{ex}/d(1/R_{cy}) < 0$, which means an unstable solution, i.e., free-energy barrier states between stable and metastable phases. With increasing μ , the f_{ex} width of the coexistence increases, and the range of f_{ex} is shifted outward (see Fig. 7). At small spontaneous curvatures ($C_0 R_0 \lesssim 200$), the transition at a small f_{ex} disappears, since it moves into the unphysical region ($f_{ex} < 0$). Although the transition at $f_{ex} < f_s$ has been previously reported in Ref. 12, the reentrant transition at $f_{ex} > f_s$ has not yet been reported. These transitions are similar to the budding transition

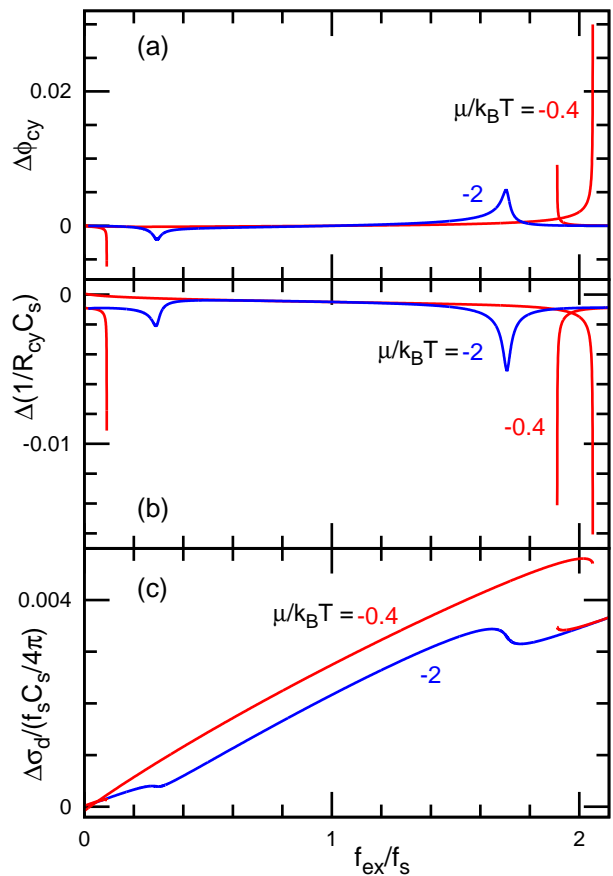


FIG. 10. Accuracy of the limit analysis using Eqs. (15)–(20) for $\mu/k_B T = -2$ and -0.4 at $C_0 R_0 = 400$, $v_r = 0.9$, $\kappa_p/\kappa_d = 3$, and $b = 0$. (a) Difference of protein density $\Delta\phi_{cy} = \phi_{cy} - \phi_{cy}^{\text{lim}}$. (b) Difference of the curvature of cylindrical membrane $\Delta(1/R_{cy} C_s) = 1/R_{cy} C_s - 1/R_{cy}^{\text{lim}} C_s$. (c) Difference of the surface tension $\Delta\sigma_d = \sigma_d - \sigma_d^{\text{lim}}$. The superscript lim represents data obtained by the limit analysis. The thermal equilibrium and metastable states are used for $\mu/k_B T = -0.4$.

between a small number of large buds and a large number of small buds [22]. However, one of the specific features of the present case is that the transitions occur twice with increasing force. This is because tubes with larger curvatures than C_s are generated by large external forces, unlike spontaneous budding.

The density ϕ_{sp} of the spherical component follows the sigmoid function $1/\{1 + \exp[-(\mu - \mu_{\text{half}})/k_B T]\}$, as shown in Figs. 4 and 6. Since changes in the radius R_{sp} are very small (see Figs. 8(b) and (c)), the deviation from this sigmoid function is negligibly small. In contrast, $\phi_{cy} - \mu$ curves can largely deviate from the sigmoid function accompanied by changes in R_{cy} (see Figs. 4 and 6). Interestingly, the proteins can bind more onto the spherical component than onto the cylindrical tube as shown in Fig. 6(a). This occurs in tubes that are narrower than $1/C_s$ at large f_{ex} values.

With increasing force f_{ex} , the surface tension σ_d and

osmotic pressure Π increase together. For $\phi_{\text{cy}} = 0$ at a low μ , $\sigma_{\text{d}} = f_{\text{ex}}/4\pi R_{\text{cy}}$ is obtained. At larger ϕ_{cy} (due to large μ), σ_{d} and Π slightly increase (see Figs. 2(c) and (d)). The vesicle ruptures when σ_{d} overcomes the lysis tension, which is typically 1–25 mN/m, depending on the membrane composition and conditions [43–45]. Since the maximum value in Fig. 2(c) is $\sigma_{\text{d}} \simeq 0.08$ mN/m, the lipid membranes are not yet ruptured in this range. However, the tubular membranes may become unstable. The minimum radius of the tubular membranes is ~ 10 nm, depending on the membrane composition. In the right end regions in Figs. 2 and 5, the tubular membrane can be ruptured or the tubular radius is saturated to a finite value due to the repulsion between membranes: For $C_0 R_0 = 400$, $R_{\text{cy}} = 1/2C_s \simeq 8$ nm and for $C_0 R_0 = 100$, $R_{\text{cy}} = 1/5C_s \simeq 13$ nm.

As the bending rigidity κ_{p} of the bound membrane increases, the slope of $1/R_{\text{cy}}-f_{\text{ex}}$ curves at $\phi_{\text{cy}} = 1$ decreases, and the first-order transitions start at a lower $\phi_{\text{cy}}^{\text{max}}$ (see Fig. 7(b)). As the reduced volume v_{r} decreases, the tube length L_{cy} increases owing to the larger available area of the tube (see Fig. 8(a)). However, the tube radius R_{cy} remains almost unchanged.

Next, we consider the inter-protein interactions ($b \neq 0$). As b decreases, protein binding is promoted at large ϕ (Figs. 9(a),(b)), such that the coexistence region widens (Fig. 9(c)). The reflection and point symmetries of the $\phi_{\text{cy}}-f_{\text{ex}}$ and $1/R_{\text{cy}}-f_{\text{ex}}$ curves (Figs. 2(a) and (b)) remain unchanged for $b \neq 0$, respectively (data not shown). Note that the membrane exhibits a phase separation with large and small ϕ within each component at $b < -2k_{\text{B}}T/a_{\text{p}}$, in which F_{sp} and F_{cy} can have double minima [22]. Thus, we only consider $b > -2k_{\text{B}}T/a_{\text{p}}$ in this study.

To confirm the quality of the limit analysis, the deviations of ϕ_{cy} , $1/R_{\text{cy}}$, and σ_{d} are shown in Fig. 10. All of these are very small. Note that the larger values at the ends of the curves in Figs. 10(a) and (b) are due to slight shifts in the spinodal points along f_{ex} . Thus, this method provides an accurate approximation, so that one can focus only on the cylindrical component to study the protein binding on the tethered vesicle. In the next section, we simulate only the membrane tubes.

III. SIMULATION OF MEMBRANE TUBES

A. Simulation Model

A fluid membrane is represented by a self-assembled single-layer sheet of N particles. The position and orientational vectors of the i -th particle are \mathbf{r}_i and \mathbf{u}_i , respectively. The details of the spin meshless membrane model are described in Ref. 27, and the combination with the protein binding is described in Ref. 29; the model is described briefly here.

The membrane particles interact with each other via the potential $U = U_{\text{rep}} + U_{\text{att}} + U_{\text{bend}} + U_{\text{tilt}}$. The potential U_{rep} is an excluded volume interaction with diameter

σ for all pairs of particles. The solvent is implicitly accounted for by the effective attractive potential U_{att} . The bending and tilt potentials are given as follows:

$$\frac{U_{\text{bend}}}{k_{\text{B}}T} = \frac{k_{\text{bend}}}{2} \sum_{i < j} (\mathbf{u}_i - \mathbf{u}_j - C_{\text{bd}} \hat{\mathbf{r}}_{i,j})^2 w_{\text{cv}}(r_{i,j}), \quad (21)$$

$$\frac{U_{\text{tilt}}}{k_{\text{B}}T} = \frac{k_{\text{tilt}}}{2} \sum_{i < j} [(\mathbf{u}_i \cdot \hat{\mathbf{r}}_{i,j})^2 + (\mathbf{u}_j \cdot \hat{\mathbf{r}}_{i,j})^2] w_{\text{cv}}(r_{i,j}), \quad (22)$$

respectively, where $\hat{\mathbf{r}}_{i,j} = \mathbf{r}_{i,j}/r_{i,j}$, $\mathbf{r}_{i,j} = \mathbf{r}_i - \mathbf{r}_j$, and $w_{\text{cv}}(r_{i,j})$ is a weight function. The spontaneous curvature is given by $C_0 = C_{\text{bd}}/2\sigma$ [27].

Each membrane particle is a binding site and takes two states (bound and unbound). In this study, $C_0 = 0$ and $k_{\text{bend}} = k_{\text{tilt}} = 10$ for the unbound membrane particles and $k_{\text{bend}} = k_{\text{tilt}} = 40$ for the bound membrane particles, where $\kappa_{\text{d}}/k_{\text{B}}T = 16 \pm 1$ and $\kappa_{\text{p}}/k_{\text{B}}T = 71 \pm 3$. In the bending and tilt potentials, for a pair of neighboring bound and unbound particles, we use the mean value $k_{\text{bend}} = k_{\text{tilt}} = 25$. For the bound membrane, $C_0\sigma = 0.05$ and 0.075 are used. The ratio of the Gaussian modulus $\bar{\kappa}$ to κ is constant as follows: $\bar{\kappa}/\kappa = -0.9 \pm 0.1$ [36]. The other parameters are the same as those used in Ref. 29. For the unbound and bound particles, the membrane areas per particle are $1.251\sigma^2$ and $1.262\sigma^2$, respectively, for tensionless membranes at $C_0 = 0$.

A tubular membrane consisting of N particles is set along the x -axis connected by the periodic boundary condition. The force f_{ex} is imposed along the x -axis, such that the tube length fluctuates thermally. Since the solvent is not explicitly taken into account, the volume of the membrane tube can freely change, as assumed in the limit analysis. We mainly used $N = 2400$. In addition, four-fold longer tubes with $N = 9600$ were used at several parameter sets, to examine finite-size effects. For $f_{\text{ex}} = 0$, $N = 19200$ was also used. Membrane motion is solved by molecular dynamics with a Langevin thermostat [46–49]. The bound and unbound states are stochastically switched by a Metropolis Monte Carlo procedure with $\Delta H = \Delta U - \mu_{\text{ms}}$, where ΔU is the energy difference between the bound and unbound states and μ_{ms} is the binding chemical potential of the membrane particles [29]. Error bars are estimated from three independent runs.

B. Simulation Results

Simulation results are shown in Figs. 11–13. As f_{ex} increases, the protein density ϕ_{cy} and tube radius R_{cy} decrease. For $\mu_{\text{ms}}/k_{\text{B}}T = 3$ and 3.5 at $C_0\sigma = 0.05$, two states (large R_{cy} with high ϕ_{cy} and small R_{cy} with low ϕ_{cy}) coexist (see Figs. 11(a), (b), and 12). These results show very good agreement with the results of the mean-field theory with the following parameter sets (see Figs. 12 and 13). Since the binding/unbinding processes in the simulation involve the energy change in the other potentials (U_{rep} and U_{att}) via a small area

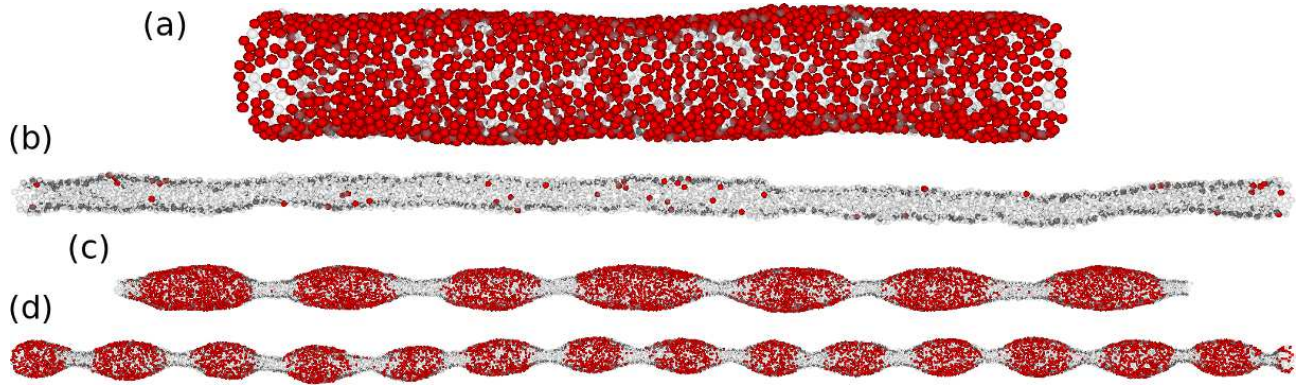


FIG. 11. Snapshots of the meshless membrane simulations at (a),(b) $N = 2400$ and (c),(d) $N = 9600$. (a),(b) At $f_{\text{ex}}\sigma/k_{\text{B}}T = 43$, $\mu_{\text{ms}}/k_{\text{B}}T = 3.5$, and $C_0\sigma = 0.05$, (a) a wide tube with a high protein density and (b) narrow tube with a low protein density coexist. (c),(d) Phase-separated membranes for (c) $C_0\sigma = 0.05$ and (d) $C_0\sigma = 0.075$ at $f_{\text{ex}}\sigma/k_{\text{B}}T = 38$ and $\mu_{\text{ms}}/k_{\text{B}}T = 3$. Red and transparent gray spheres represent the bound and unbound membrane particles, respectively.

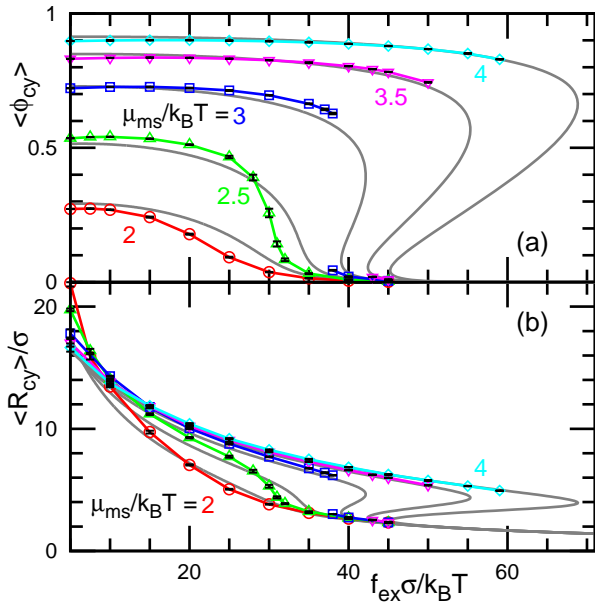


FIG. 12. Tubular membranes for $\mu_{\text{ms}}/k_{\text{B}}T = 2, 2.5, 3, 3.5$, and 4 at $C_0\sigma = 0.05$. (a) Protein density ϕ_{cy} . (b) Tube radius R_{cy} . The symbols with solid lines represent simulation data, and the gray lines represent the prediction of the mean-field theory at $\mu = \mu_{\text{ms}} - 3.5k_{\text{B}}T$ and $ba_{\text{p}}/k_{\text{B}}T = -1$.

change, the chemical potential is shifted from the input value μ_{ms} [29]. Thus, we use $\mu = \mu - 3.5k_{\text{B}}T$ and $\mu - 3.8k_{\text{B}}T$ with $a_{\text{p}} = 1.2\sigma^2$ for $C_0\sigma = 0.05$ and 0.075, respectively. In the simulation, no direct interactions are considered between the bound sites. However, the Casimir-like attractive interactions occur between them owing to the bending rigidity difference [29]. To mimic this, $ba_{\text{p}}/k_{\text{B}}T = -1$ is used here. In the theory, ϕ_{cy} has a maximum at $f_{\text{ex}} = f_{\text{s}}$ ($f_{\text{s}}\sigma/k_{\text{B}}T = 6.5$ and 9.7 for $C_0\sigma = 0.05$ and 0.075, respectively). Indeed, $\phi_{\text{cy}}^{\text{max}}$ is obtained at $f_{\text{ex}} \simeq f_{\text{s}}$ in the simulation for $\phi_{\text{cy}}^{\text{max}} \lesssim 0.5$ at $\mu = 2k_{\text{B}}T$; however, it slightly increases with increasing

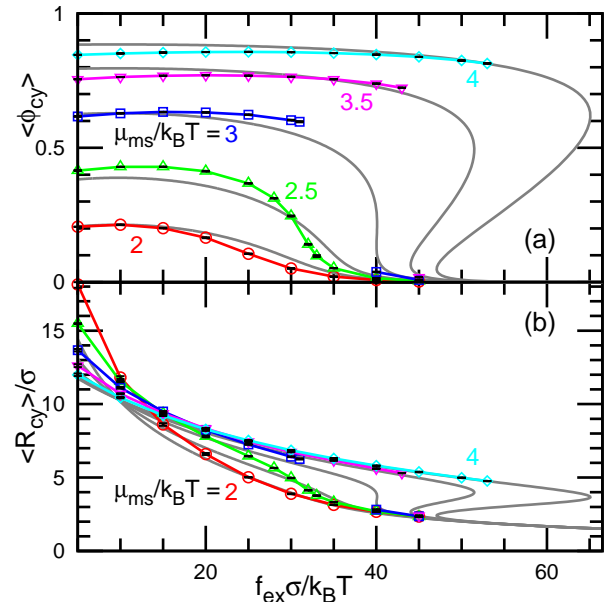


FIG. 13. Tubular membranes for $\mu_{\text{ms}}/k_{\text{B}}T = 2, 2.5, 3, 3.5$, and 4 at $C_0\sigma = 0.075$. (a) Protein density ϕ_{cy} . (b) Tube radius R_{cy} . The symbols with solid lines represent simulation data, and the gray lines represent the prediction of the mean-field theory at $\mu = \mu_{\text{ms}} - 3.8k_{\text{B}}T$ and $ba_{\text{p}}/k_{\text{B}}T = -1$.

μ to $f_{\text{ex}} \simeq 2f_{\text{s}}$ at $\mu_{\text{ms}} = 4k_{\text{B}}T$. Because the Casimir-like forces are not pairwise, their multibody interactions likely induce this dependency. At a small force f_{ex} and low ϕ_{cy} , the radius R_{cy} calculated by the simulation is slightly larger than the theoretical prediction. This is due to the thermal undulation of the membrane. Except for these, the simulation results are well reproduced.

Homogeneous membrane tubes are not maintained in some ranges of the simulation parameters. First, the membrane tubes become unstable at large and small limits of f_{ex} . The membranes are ruptured for radii that are too small $R_{\text{cy}} \lesssim 2\sigma$ at large f_{ex} . At $f_{\text{ex}} = 0$, the tubular

membrane becomes divided into vesicles through unduloid shapes [50, 51], in which a constant value of the mean curvature H is maintained everywhere. The cylindrical tube at $f_{\text{ex}} = 0$ has the curvature of the curvature generation, as $1/R_{\text{cy}} = 2H_{\text{g}} = \kappa_{\text{p}}\langle\phi_{\text{cy}}\rangle C_0 / (\kappa_{\text{dif}}\langle\phi_{\text{cy}}\rangle + \kappa_{\text{d}})$ from Eq. (18). However, longer tubes than the unduloid wavelength $l_{\text{und}} = 2\pi R_{\text{cy}}$ (large μ at $N = 9600$ and 19200) deform into unduloid shapes, and subsequent membrane fission at the narrow neck of the tube leads to the formation of spherical vesicles (see Movie 1 provided in ESI for $\mu = 4k_{\text{B}}T$, $C_0\sigma = 0.075$, and $N = 19200$). Cylindrical shapes maintain for shorter tubes than the unduloid wavelength owing to the finite-size effect.

In addition, phase separation can destabilize cylindrical shapes. A beaded-necklace-like tube with phase separation is formed in the middle-density region ($0.2 \lesssim \phi_{\text{cy}} \lesssim 0.5$) around the critical points (see Figs. 11(c) and (d)). The bound membranes form an ellipsoidal shape, whereas the unbound membranes form a saddle shape between them. In Figs. 12 and 13, the data of the phase-separated tubes are not plotted. The homogeneous phases disappear for $3.2 \lesssim f_{\text{ex}}\sigma/k_{\text{B}}T \lesssim 3.9$ at $C_0\sigma = 0.075$ and $\mu_{\text{ms}}/k_{\text{B}}T = 3$ (see Figs. 11(c) and Movie 2 provided in ESI using the same parameter set with different initial conformations). This beaded-necklace-like tube is also formed when the homogeneous tube becomes unstable at the ends of the metastable state of the coexistence region (see Figs. 11(d)). The coexistence region is narrower in the simulation than in the theory. The phase separation likely causes this reduction of the coexistence region.

Similar necklace-like membrane tubes with phase separation have been previously observed in the experiments on three-component membranes [52, 53]. In their system, the difference in bending rigidity causes a neck-like shape. In contrast, for the present system, the difference in the spontaneous curvature gives more dominant effects. Unduloid-like deformations have been reported in tethered vesicles after force release [54], as well as in tubular vesicles with polymer anchoring [55] and rolled membranes during detachment from a substrate [37]. In contrast, phase separation can make cylindrical tubes unstable under strong forces.

Although Fig. 11 shows only necklace-like membranes of longer tubes, the shorter tubes with $N = 2400$ also show this structure with fewer periodicities (one or two circular bumps). The simulation results exhibit no notable differences between these two tube sizes, except for slightly wider coexistence regions for the shorter tubes.

Here, we used a constant chemical potential and constant external force. The same membrane shapes can be obtained with the ensemble of a constant number N_{p} of the proteins and/or constant tube length L_{cy} , when the condition is adjusted. Note that for fixed N_{p} or L_{cy} , phase separation appears more often in the regions of the first-order transitions owing to the macroscopic phase separation. For example, at $\phi_{\text{cy}} \simeq 0.4$ and $f_{\text{ex}}\sigma/k_{\text{B}}T > 40$, no solution exists in Figs. 12 and 13.

Thus, when $N_{\text{p}}/N = 0.4$, the membrane is separated into two regions of high and low protein densities. This is similar to the gas-liquid coexistence in the NVT ensemble [56].

IV. SUMMARY AND DISCUSSIONS

We have studied the binding of curvature-inducing proteins onto the tethered vesicle. Proteins exhibit an isotropic spontaneous curvature such that they sense and generate the curvature of membranes. For a completely unbound membrane, the tube curvature and tube length are proportional to the force strength. As the binding chemical potential increases, the protein density sigmoidally increases in the spherical component of the vesicle. In contrast, a discrete increase can also occur in the membrane tube, accompanied by a change in the tube radius. The force-density curve and force-tube-curvature curve are reflection and point symmetric to the point, where the tube curvature equals to the sensing curvature, respectively. The approximation that neglects the tube volume for a small tube radius well reproduces the results of the analysis for a finite volume. Meshless simulations of membrane tubes were conducted to confirm these theoretical results. The results of the simulation and theory for the homogeneous phases show very good agreement. Additionally, in the simulation, beaded-necklace-like membrane tubes with phase separation are found around the critical points. Membrane deformation induces this microphase separation.

Based on these mean-field analyses, we propose a method for estimating the bending rigidity change by protein binding. The sensing curvature is obtained as the tube curvature at the maximum protein density under variation in the tube radius. The bending rigidity ratio is obtained from the slope of $d(1/R_{\text{cy}})/df_{\text{ex}}$ at this maximum protein density as expressed in Eq. (19). The maximum density can be varied by the binding chemical potential μ , which is a function of the buffer protein concentration ρ . For a dilute solution, $\mu(\rho) = \mu(1) + k_{\text{B}}T \ln(\rho)$.

In this study, we consider only proteins that isotropically bend the membrane and have no preferred lateral direction. The BAR superfamily proteins exhibit anisotropic spontaneous curvatures. Previously, we have reported that such proteins show characteristic behavior in tubular membranes [28, 30, 31, 35]; the force-protein-curvature curve has a flat region at low curvature owing to the adjustment of the protein orientation, and protein assembly induces elliptic and polyhedral tube formations. However, the mean-field theory of the isotropic spontaneous curvature has been used to analyze the experimental results on the binding of the BAR proteins to the tethered membranes [12]. Recently, a mean-field theory for a nematic order coupled with protein bending energy was developed for a fixed-shaped membrane [57]. The present method can be extended to anisotropic proteins by including the orientational degree. This is one

of the directions for further studies.

ACKNOWLEDGMENTS

This work was supported by JSPS KAKENHI Grant Number JP21K03481.

-
- [1] H. T. McMahon and J. L. Gallop, *Nature* **438**, 590 (2005).
- [2] S. Suetsugu, S. Kurisu, and T. Takenawa, *Physiol. Rev.* **94**, 1219 (2014).
- [3] L. Johannes, R. G. Parton, P. Bassereau, and S. Mayor, *Nat. Rev. Mol. Cell Biol.* **16**, 311 (2015).
- [4] F. Brandizzi and C. Barlowe, *Nat. Rev. Mol. Cell Biol.* **14**, 382 (2013).
- [5] J. H. Hurley, E. Boura, L.-A. Carlson, and B. Rózycki, *Cell* **143**, 875 (2010).
- [6] H. T. McMahon and E. Boucrot, *Nat. Rev. Mol. Cell Biol.* **12**, 517 (2011).
- [7] T. Itoh and P. De Camilli, *Biochim. Biophys. Acta* **1761**, 897 (2006).
- [8] C. Mim and V. M. Unger, *Trends Biochem. Sci.* **37**, 526 (2012).
- [9] R. Dimova, *Adv. Colloid Interface Sci.* **208**, 225 (2014).
- [10] T. Baumgart, B. R. Capraro, C. Zhu, and S. L. Das, *Annu. Rev. Phys. Chem.* **62**, 483 (2011).
- [11] B. Sorre, A. Callan-Jones, J. Manzi, B. Goud, J. Prost, P. Bassereau, and A. Roux, *Proc. Natl. Acad. Sci. USA* **109**, 173 (2012).
- [12] C. Prévost, H. Zhao, J. Manzi, E. Lemichez, P. Lapalainen, A. Callan-Jones, and P. Bassereau, *Nat. Commun.* **6**, 8529 (2015).
- [13] A. Roux, G. Koster, M. Lenz, B. Sorre, J.-B. Manneville, P. Nassoy, and P. Bassereau, *Proc. Natl. Acad. Sci. USA* **107**, 4141 (2010).
- [14] K. R. Rosholm, N. Leijnse, A. Mantsiou, V. Tkach, S. L. Pedersen, V. F. Wirth, L. B. Oddershede, K. J. Jensen, K. L. Martinez, N. S. Hatzakis, P. M. Bendix, A. Callan-Jones, and D. Stamou, *Nat. Chem. Biol.* **13**, 724 (2017).
- [15] A. Allard, M. Bouzid, T. Betz, C. Simon, M. Abou-Ghali, J. Lemière, F. Valentino, J. Manzi, F. Brochard-Wyart, K. Guevorkian, J. Plastino, M. Lenz, C. Campillo, and C. Sykes, *Sci. Adv.* **6**, eaaz3050 (2020).
- [16] H. Hotani, F. Nomura, and Y. Suzuki, *Curr. Opin. Coll. Interface Sci.* **4**, 358 (1999).
- [17] T. Inaba, A. Ishijima, M. Honda, F. Nomura, K. Takiguchi, and H. Hotani, *J. Mol. Biol.* **348**, 325 (2005).
- [18] Z. Wu, H. Yuan, X. Zhang, and X. Yi, *Soft Matter* **11**, 2552 (2016).
- [19] K. Gavriljuk, B. Scocozza, F. Ghasemalizadeh, H. Seidel, A. P. Nandan, M. Campos-Medina, M. Schmick, A. Koseska, and P. I. H. Bastiaens, *Nat. Commun.* **12**, 1548 (2021).
- [20] T. Svitkina, *Cold Spring Harb. Perspect. Biol.* **10**, a018267 (2018).
- [21] J. L. Gallop, *Semin. Cell Dev. Biol.* **102**, 81 (2020).
- [22] H. Noguchi, *Phys. Rev. E* **104**, 014410 (2021).
- [23] M. Müller, K. Katsov, and M. Schick, *Phys. Rep.* **434**, 113 (2006).
- [24] M. Venturoli, M. M. Sperotto, M. Kranenburg, and B. Smit, *Phys. Rep.* **437**, 1 (2006).
- [25] H. Noguchi, *J. Phys. Soc. Jpn.* **78**, 041007 (2009).
- [26] H. Noguchi and G. Gompper, *Phys. Rev. E* **73**, 021903 (2006).
- [27] H. Shiba and H. Noguchi, *Phys. Rev. E* **84**, 031926 (2011).
- [28] H. Noguchi, *Phys. Rev. E* **93**, 052404 (2016).
- [29] Q. Goutaland, F. van Wijland, J.-B. Fournier, and H. Noguchi, *Soft Matter* **17**, 5560 (2021).
- [30] H. Noguchi, *EPL* **108**, 48001 (2014).
- [31] H. Noguchi, *J. Chem. Phys.* **143**, 243109 (2015).
- [32] H. Noguchi, *Sci. Rep.* **6**, 20935 (2016).
- [33] H. Noguchi and J.-B. Fournier, *Soft Matter* **13**, 4099 (2017).
- [34] H. Noguchi, *Soft Matter* **13**, 7771 (2017).
- [35] H. Noguchi, *Sci. Rep.* **9**, 11721 (2019).
- [36] H. Noguchi, *J. Chem. Phys.* **151**, 094903 (2019).
- [37] H. Noguchi, *Soft Matter* **15**, 8741 (2019).
- [38] A.-S. Smith, E. Sackmann, and U. Seifert, *Phys. Rev. Lett.* **92**, 208101 (2004).
- [39] T. R. Powers, G. Huber, and R. E. Goldstein, *Phys. Rev. E* **65**, 041901 (2002).
- [40] L. Bo and R. Waugh, *Biophys. J.* **55**, 509 (1989).
- [41] E. Evans, H. Bowman, A. Leung, D. Needham, and D. Tirrell, *Science* **273**, 933 (1996).
- [42] D. Cuvelier, I. Derényi, P. Bassereau, and P. Nassoy, *Biophys. J.* **88**, 2714 (2005).
- [43] E. A. Evans and F. Ludwig, *J. Phys. Condens. Matter* **12**, A315 (2000).
- [44] E. A. Evans, V. Heinrich, F. Ludwig, and W. Rawicz, *Biophys. J.* **85**, 2342 (2003).
- [45] H. V. Ly and M. L. Longo, *Biophys. J.* **87**, 1013 (2004).
- [46] M. P. Allen and D. J. Tildesley, *Computer Simulation of Liquids* (Clarendon Press, Oxford, 1987).
- [47] S. E. Feller, Y. Zhang, R. W. Pastor, and B. R. Brooks, *J. Chem. Phys.* **103**, 4613 (1995).
- [48] H. Noguchi, *J. Chem. Phys.* **134**, 055101 (2011).
- [49] H. Noguchi, *Soft Matter* **8**, 3146 (2012).
- [50] K. Kenmotsu, *Surfaces with constant mean curvature* (American Mathematical Society, Providence, R.I., 2003).
- [51] H. Naito, M. Okuda, and O.-Y. Zhong-can, *Phys. Rev. Lett.* **74**, 4345 (1995).
- [52] M. Yanagisawa, M. Imai, and T. Taniguchi, *Phys. Rev. Lett.* **100**, 148102 (2008).
- [53] M. Yanagisawa, M. Imai, and T. Taniguchi, *Phys. Rev. E* **82**, 051928 (2010).
- [54] C. Tozzi, N. Walani, and M. Arroyo, *New J. Phys.* **21**, 093004 (2019).
- [55] I. Tsafrir, D. Sagi, T. Arzi, M.-A. Guedeau-Boudeville,

- V. Frette, D. Kandel, and J. Stavans, *Phys. Rev. Lett.* **86**, 1138 (2001).
- [56] H. Watanabe, N. Ito, and C.-K. Hu, *J. Chem. Phys.* **136**, 204102 (2012).
- [57] C. Tozzi, N. Walani, A.-L. L. Roux, P. Roca-Cusachs, and M. Arroyo, *Soft Matter* **17**, 3367 (2021).